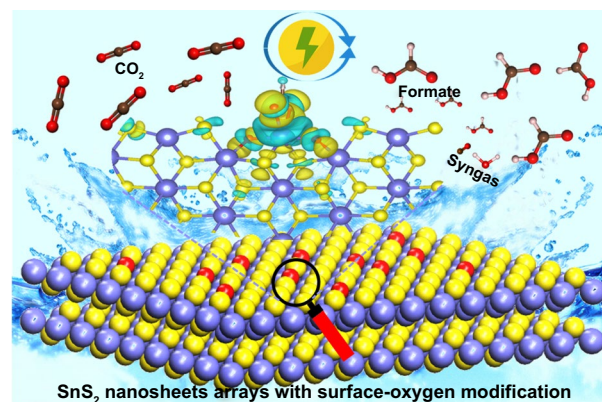# Surface Oxygen Injection in Tin Disulfide Nanosheets for Efficient CO_2 Electroreduction to Formate and Syngas

Tao Chen[1,2], Tong Liu[1], Tao Ding[1], Beibei Pang[1], Lan Wang[1,2], Xiaokang Liu[1], Xinyi Shen[1], Sicong Wang[1], Dan Wu[1], Dong Liu[1], Linlin Cao[1], Qiquan Luo[3], Wei Zhang[1,4] ✉, Wenkun Zhu[2] ✉, Tao Yao[1] ✉

HIGHLIGHTS

- A surface oxygen-injection strategy is proposed to synergistically modulate the electronic structure of the SnS_2 nanosheets, thereby regulating the oxophilicity of the catalyst surface.

- The surface oxygen doping facilitates the CO_2 activation and enhances the affinity for HCOO* species.

- The oxygen-injection SnS_2 nanosheets exhibit a remarkable Faradaic efficiency of 91.6% for carbonaceous products with a current density of 24.1 mA cm^{-2} at -0.9 V vs RHE.

ABSTRACT Surface chemistry modification represents a promising strategy to tailor the adsorption and activation of reaction intermediates for enhancing activity. Herein, we designed a surface oxygen-injection strategy to tune the electronic structure of SnS_2 nanosheets, which showed effectively enhanced electrocatalytic activity and selectivity of CO_2 reduction to formate and syngas (CO and H_2). The oxygen-injection SnS_2 nanosheets exhibit a remarkable Faradaic efficiency of 91.6% for carbonaceous products with a current density of 24.1 mA cm^{-2} at −0.9 V vs RHE, including 83.2% for formate production and 16.5% for syngas with the CO/H_2 ratio of 1:1. By *operando* X-ray absorption spectroscopy, we unravel the in situ surface oxygen doping into the matrix during reaction, thereby optimizing the Sn local electronic states. *Operando* synchrotron radiation infrared spectroscopy along with theoretical calculations further reveals that the surface oxygen doping facilitated the CO_2 activation and enhanced the affinity for HCOO* species. This result demonstrates the potential strategy of surface oxygen injection for the rational design of advanced catalysts for CO_2 electroreduction.

SnS_2 nanosheets arrays with surface-oxygen modification

KEYWORDS Oxygen injection; Tin disulfide; CO_2 electroreduction; Formate; Syngas

Tao Chen and Tong Liu contributed equally to this work.

✉ Wei Zhang, zwei2319@mail.ustc.edu.cn; Wenkun Zhu, zhuwenkun@swust.edu.cn; Tao Yao, yaot@ustc.edu.cn

1 National Synchrotron Radiation Laboratory, University of Science and Technology of China, Hefei 230029, People's Republic of China
2 State Key Laboratory of Environmentally Friendly Energy Materials, School of National Defense Science and Technology, Southwest University of Science and Technology, Mianyang 621010, People's Republic of China
3 Institutes of Physical Science and Information Technology, Anhui University, Hefei 230601, People's Republic of China
4 School of Materials, Sun Yat-Sen University, Guangzhou 510275, People's Republic of China

1 Introduction

Electroreduction of carbon dioxide (CO_2RR) into high-value fuels and feedstocks offers a compelling pathway not only to meet the increasing energy demand, but also to alleviate the environmental crisis caused by CO_2 emissions [1–3]. According to the gross-margin model, formate is considered to be one of the most economically feasible products in the CO_2RR, which can be widely used as an important raw material in the chemical and pharmaceutical industries, as well as a potential hydrogen carrier and the liquid fuel for proton-exchange membrane fuel cell [4–6]. Up to now, various metal-based electrocatalysts, such as Pd, In, Hg, Pb, Cd, and Sn, have been exploited to achieve the CO_2 electroreduction to formate [7–13]. Among these electrocatalysts, Sn-based materials have attracted considerable attention due to their advantages of earth abundance, non-toxicity, and low cost. Unfortunately, the catalytic performance of most Sn-based materials is still limited by the high energy barrier for CO_2 activation, which is usually attributed to the poor stabilization of CO_2*$^-$ intermediates [14–18]. To this end, it is of great significance to develop an efficient and durable Sn-based catalysts for the CO_2 electroreduction to formate.

Given that the CO_2 molecule activation is closely related to the number and inherent activity of active sites, many effective strategies have been employed to tailor the active sites of electrocatalysts for enhancing the efficiency of the CO_2 electroreduction to formate [19–21]. The surface chemistry modification, as a powerful strategy, has attracted great interest in adjusting electronic properties of active sites to target intermediate adsorption energy as well as harvest high selectivity [22–25]. For example, Xie et al. developed a general amino acid modification approach on Cu electrodes for the selective electroreduction of CO_2 toward hydrocarbons [26]. Previous theoretical calculations have confirmed that the *OCHO binding energy is closely associated with the oxophilicity of the catalyst surface, which can be achieved by modifying the surface of the electrocatalyst with oxygen atom [27]. For instance, Gao et al. reported a phenomenon that partially oxidized atomic cobalt layers effectively adjusted the electronic structure, promoted the activation of CO_2, and stabilized the relevant key intermediates, thereby enhancing the efficiency of the CO_2 electroreduction to liquid fuel [28]. As another example, Won et al. prepared hierarchical Sn dendrites and found that the natural oxygen content is closely related to the stability of CO_2*$^-$ intermediates and the selectivity of formate [29]. To improve the catalytic performance of Sn-based materials, oxygen modification is a promising strategy to regulate the surface oxophilicity of the catalysts and further manipulate their electronic structure. In fact, most of the catalysts with surface chemical modification have undergone structural evolution of the active phase under operation conditions, leading to deviations in the understanding the nature of the active site. Therefore, monitoring the structural evolution of Sn-based catalysts with surface oxygen modification under realistic working conditions is crucial for understanding the nature of the active phase and the rational design of targeted CO_2RR catalysts.

Herein, the SnS_2 nanosheets arrays on the carbon paper with surface oxygen modification were rationally designed under the guidance of density function theory (DFT) to effectively electroreduce CO_2 into formate and syngas (CO and H_2). The introduction of oxygen into the surface of SnS_2 nanosheets achieved the exposure of Sn active sites and optimal Sn electronic states, thereby enhancing the adsorption and activation of CO_2. Specifically, the SnS_2 nanosheets with surface oxygen modification exhibit a remarkable Faradaic efficiency of 91.6% for carbonaceous products at −0.9 V vs RHE, including 83.2% for formate production and 16.5% for syngas with the CO/H_2 ratio of 1:1. Operando X-ray absorption spectroscopy unravels that the in situ surface oxygen doping into the matrix under working conditions effectively changes the local electronic state of Sn, thereby providing an optimized electronic structure to improve CO_2RR performance. In addition, operando synchrotron radiation infrared spectroscopy and DFT calculations further confirm that the local electronic state of Sn is manipulated through surface oxygen modification, thereby promoting the CO_2 activation and enhancing the affinity for HCOO* species.

2 Experimental Section

The experimental details are provided in Supporting Information (SI). This section briefly summarizes the synthesis measurements.

In a typical synthesis of $SnS_{2-x}O_x$/CC, 5 mmol of $SnCl_4·5H_2O$ and 15 mmol of thioacetamide were dissolved in 40 mL of deionized water. The mixture and carbon paper (2×2) were then transferred into a Teflon-lined

stainless-steel autoclave, followed by being heated to 190 °C for 8 h. After the mixture was cooled down naturally to room temperature, the SnS_2/CC was washed by water three times and ethanol twice to remove any possible ions, followed by being dried under vacuum at 60 °C for 12 h. The $SnS_{2-x}O_x$/CC was prepared by placing the SnS_2/CC in the muffle furnace that had been heated at 300 °C for several minutes.

3 Results and Discussion

### 3.1 Preparation and Characterization of $SnS_{2-x}O_x$/CC

At first, to gain insight into the effect of surface oxygen-injection engineering on electronic properties of SnS_2 nanosheets, we conducted DFT calculations by using the SnS_2 slab with/without oxygen injection as the models (Fig. 1a, b). Compared with the pristine SnS_2, the surface oxygen injection leads to a new additional state near the Fermi level (Fig. 1c, d), which is beneficial to manipulate the local electronic structure of Sn and expose the active site of Sn at the edges. Notably, O 2*p* states also contributed the unoccupied part of these levels, making them serve as the highly catalytically active sites. Furthermore, the electronic localization functions (ELF) exhibit that the charge density is mainly derived from the S atoms for both the SnS_2 with/without oxygen injection (Fig. S1). Owing to the introduction of oxygen atoms, the electron density of the whole system has undergone distinctly change, further indicating surface oxygen injection effectively tailors the local electronic structure of Sn.

Then, the SnS_2 nanosheets arrays with partially oxidized surface on the carbon paper (denoted as $SnS_{2-x}O_x$/CC) were prepared, as schematically illustrated in Fig. 2a. Specifically, the pristine SnS_2 nanosheets arrays were directly grown on the carbon paper by a simple hydrothermal method. Afterward, the $SnS_{2-x}O_x$/CC was further synthesized by the low-temperature calcination of the as-prepared SnS_2/CC under the air atmosphere. The morphology of the $SnS_{2-x}O_x$/CC was characterized by scanning electron microscopy (SEM) and transmission electron microscopy (TEM). As shown in Fig. 2b, the final products present a hierarchical nanosheets arrays composed of $SnS_{2-x}O_x$ nanosheets and flexible carbon paper. The TEM images of the SnS_2 and $SnS_{2-x}O_x$ took the nanosheet morphology (Figs. 2c and S2a), whereas the SnS_2 nanosheets were completely oxidized into SnO_2

nanoplatelets (Fig. S3). The high-resolution transmission electron microscopy (HRTEM) image in Fig. 2d shows that the $SnS_{2-x}O_x$ lattice fringes with an interplanar distance of 0.32 nm indexed to the (002) facets of SnS_2, confirming the as-obtained $SnS_{2-x}O_x$ nanosheets retain its pristine crystal structure (Fig. S2b, c) [30]. Besides, there is an obvious circle of amorphous layer at the edge of the $SnS_{2-x}O_x$ nanosheet, which is attributed to the partial oxidation on the surface of the SnS_2 nanosheet. In addition, the homologous fast Fourier transform (FFT) pattern indicates the SnS_2 phase recorded from [002] orientation (inset in Fig. 2e). The element of O was uniformly distributed on the whole $SnS_{2-x}O_x$ nanosheet which can be further confirmed by the high-angle annular dark-field energy-dispersive X-ray spectroscopy (HAADF-EDS) elemental mapping and EDS spectrum (Figs. 2f and S4).

To further investigate the phase composition and electronic structure of the $SnS_{2-x}O_x$/CC, we performed X-ray diffraction (XRD) and X-ray photoelectron spectroscopy (XPS) measurement. As evidenced by the XRD patterns in Fig. S5, the SnS_2/CC and $SnS_{2-x}O_x$/CC exhibited the diffraction peaks at 30.74°, 32.09°, and 44.98°, which were indexed to the (200), (101), and (211) planes of hexagonal SnS_2 (JCPDS No. 23–0677) [31]. Remarkably, no additional peaks corresponding to the phases of SnO_2 could be found, indicating that the surface oxygen injection did not change the crystalline phase of SnS_2. We further carried out the XPS measurements to clarify the form of O existing in $SnS_{2-x}O_x$/CC. As disclosed by XPS survey spectra, a weak signal of O was recorded in $SnS_{2-x}O_x$/CC, further confirming successful introduction of O (Figs. S6 and S7). In addition, the peaks at 495.3 and 486.8 eV were attributed to Sn $3d_{3/2}$ and Sn $3d_{5/2}$ of $SnS_{2-x}O_x$/CC, respectively (Fig. S8) [32]. Compared with the SnS_2/CC, the Sn $3d_{3/2}$ and $3d_{5/2}$ peaks for $SnS_{2-x}O_x$/CC shifted to higher binding energies, due to the larger electronegativity of O than that of S.

The surface-sensitive synchrotron radiation soft X-ray absorption structure (XAS) was further employed to investigate the changes in the local electronic structure of SnS_2 caused by surface oxygen-injection engineering. As shown in Fig. S9, O *K*-edge XAS spectra for $SnS_{2-x}O_x$/CC and pure SnO_2/CC displayed similar shapes, implying SnO_2 species were formed on the surface of $SnS_{2-x}O_x$/CC, further confirming the surface oxygen injection successfully replaced the S atoms. In addition, S *L*-edge XAS spectra exhibited the two characteristic peaks located at 163.3 eV (S-Sn π*
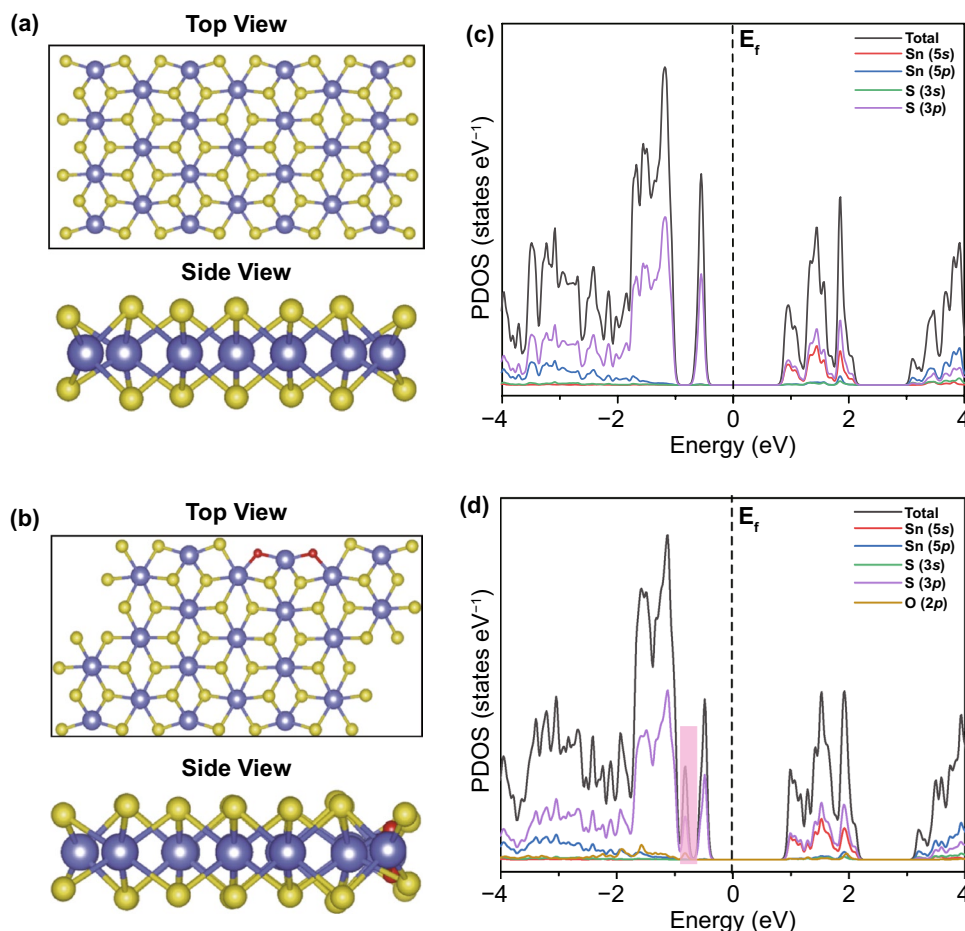
Fig. 1 Top view and side view of the model for **a** pristine SnS_2 and **b** $SnS_{2-x}O_x$. Calculated DOS of **c** SnS_2 and **d** $SnS_{2-x}O_x$ slabs

peak) and 166.6 eV (S-Sn σ* peak) observed in pure SnS_2/CC and the $SnS_{2-x}O_x$/CC (Fig. S10). Compared with pristine SnS_2/CC, the relative strength of S-Sn for $SnS_{2-x}O_x$/CC was slightly reduced, which was attributed to the substitution of partial S atoms on the surface of $SnS_{2-x}O_x$/CC by O atoms. Meanwhile, the X-ray absorption near-edge structure (XANES) measurement was employed to further investigate the effect of surface oxygen injection. Compared with pristine SnS_2/CC, the white line peak of the $SnS_{2-x}O_x$/CC shifted to the high-E region, due to the electronegativity of O being greater than that of S, in consistent with the results of Sn $3d$ XPS spectrum (Fig. S11). Given that the white line peak of Sn K-edge intensity originating from the transition of the 1 s to 5p orbital, the increase in the white line peak intensity after surface oxygen injection indicates the increases in the

possibility of electron transition from the 1 s-5p orbital. The above results reveal the surface oxygen injection effectively manipulates the local electronic structure of Sn.

Furthermore, the Fourier transform (FT) k^2-weighted extended XAFS (EXAFS) spectrum of the Sn K-edge was employed to further reveal the effect of surface oxygen injection on the local electronic structure of Sn at the atomic level. Considering the surface oxygen injection into the SnS_2 nanosheets, we performed out least-squares EXAFS curve fitting analysis for Sn by considering two backscattering paths, including Sn–S and Sn–O. Compared with the SnS_2/CC, the Sn K-edge FT-EXAFS curve for $SnS_{2-x}O_x$/CC presented a new peak at 1.49 Å, which is ascribed to the Sn–O coordination (Fig. 2a) [33]. By quantitative EXAFS curve fitting analysis, the coordination number of Sn-S for
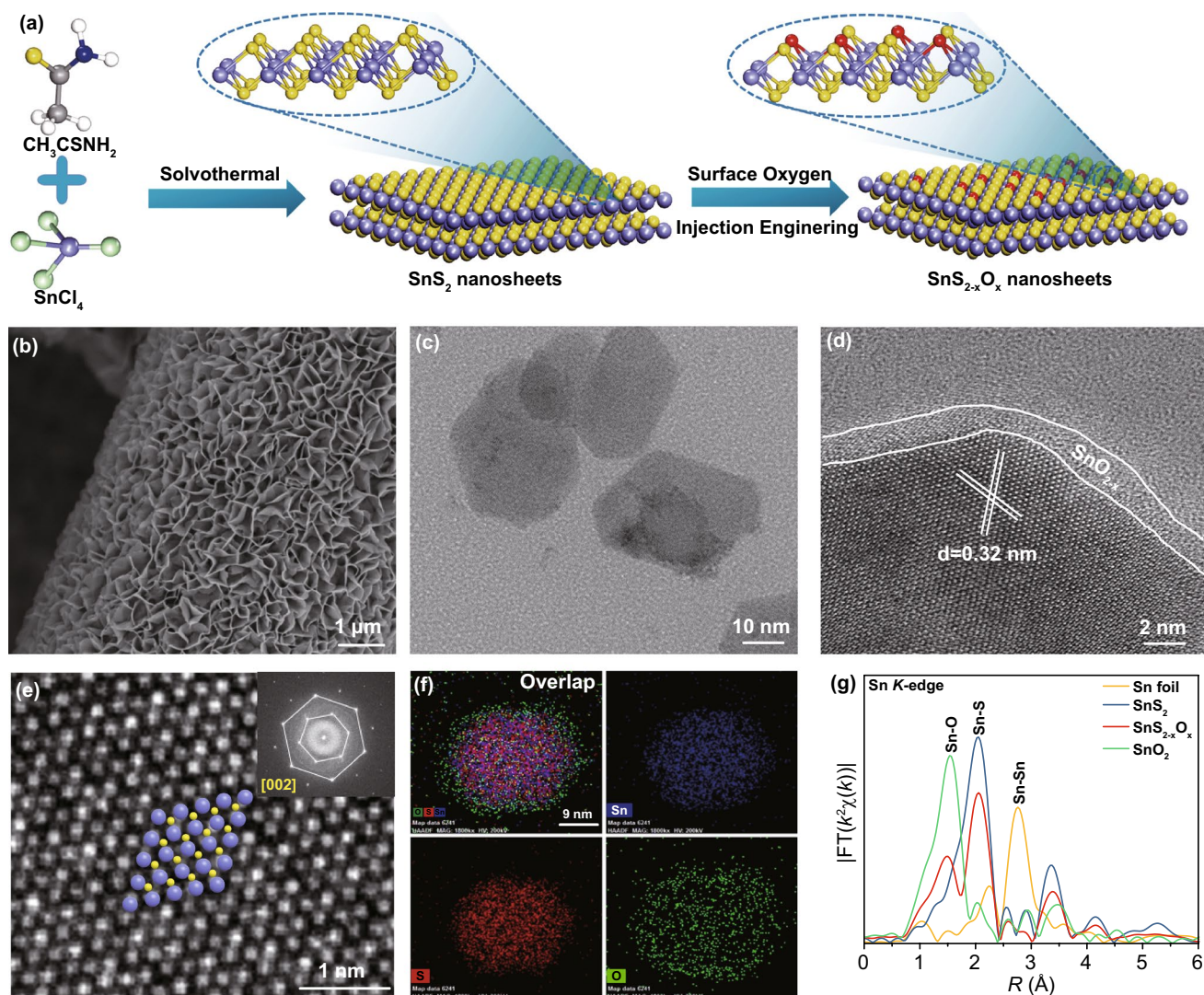
Fig. 2 a Schematic illustration of the manufacture of $SnS_{2-x}O_x$ nanosheets. **b** SEM image of $SnS_{2-x}O_x$/CC. **c** TEM image of $SnS_{2-x}O_x$ nanosheets. **d, e** HRTEM image and the homologous FFT pattern of $SnS_{2-x}O_x$ nanosheets (inset in **e**). **f** HAADF-STEM and STEM-EDX elemental mapping images of an individual $SnS_{2-x}O_x$ nanosheet. **g** Fourier transform spectra of Sn K-edge for Sn foil, SnS_2, $SnS_{2-x}O_x$, and SnO_2 from EXAFS

$SnS_{2-x}O_x$/CC is confirmed to be 4.3, smaller than that of pristine SnS_2/CC (6.0), and the coordination number of Sn–O is verified to be 2.1, further confirming surface oxygen injection successfully replaced the S atoms (Table S1 and Fig. S12). Moreover, the wavelet transform (WT) of Sn K-edge EXAFS oscillations exhibited the intensity maxima at 4.3 Å^{-1} and around 8.2 Å^{-1} of $SnS_{2-x}O_x$/CC, which associate with Sn–O and Sn–S contributions, respectively (Fig. S13). Taken together, the successful injection of surface oxygen effectively manipulated the local electronic structure of SnS_2.

3.2 Electrocatalytic CO₂RR Performances of the $SnS_{2-x}O_x$/CC

Surface oxygen-injection engineering provides a potential prospect for enhancing the CO_2 electroreduction. The electrocatalytic CO_2 reduction activities of the three Sn-based catalysts were evaluated using a three-electrode H-cell in CO_2-saturated 0.5 M $KHCO_3$. The linear sweep voltammetric (LSV) curves in Fig. S14 revealed that the $SnS_{2-x}O_x$ nanosheets exhibited higher current density than that of pristine SnS_2 nanosheets, confirming the injection

of oxygen effectively enhanced the electrocatalytic activity of SnS_2/CC. Particularly, the geometrical current density of $SnS_{2-x}O_x$/CC achieved 19.68 mA cm^{-2}, which was 2.7 times higher than that of pristine SnS_2/CC at overpotential of -0.8 V vs RHE (Fig. 2a). For these three Sn-based catalysts, H_2, CO, and formate were the main catalytic products, which are quantified by online gas chromatography and ^{1}H NMR analysis (Fig. S15). Figure 2b exhibits partial current density for carbonaceous products (CO and formate), respectively. At all applied potentials, the $SnS_{2-x}O_x$/CC presented the largest current density among the three electrocatalysts, demonstrating the high activity for CO_2 electroreduction. As shown in Fig. 2c, the $SnS_{2-x}O_x$/CC displayed the highest Faradaic efficiency (FE) for carbonaceous products among the three electrocatalysts, while the pristine SnS_2/CC exhibited the lowest FE value. At -0.9 V vs RHE, the $SnS_{2-x}O_x$/CC exhibited the FE of 91.8% for carbonaceous products, including the FE of 83.5% for formate production and the FE of 16.5% for syngas with the H_2/CO ratio of 1:1. It is worth noting that such syngas ratio is optimal for multiple chemical synthesis (e.g., Fischer–Tropsch synthesis, fermentation and alcohol synthesis, and hydroformylation processes). Furthermore, the as-prepared $SnS_{2-x}O_x$/CC displayed an excellent durability for 10-h potentiostatic test with the less than 3% decay in current density, together with the FE for formate and CO keeping steady at -0.9 V vs RHE (Fig. 2d). The above results demonstrate that the $SnS_{2-x}O_x$/CC represents a promising catalyst for persistently producing formate and syngas toward CO_2RR.

Inspired by surface oxygen injection to improve the CO_2 electroreduction performance of SnS_2/CC, we studied the microscopic reaction kinetics of the pristine SnS_2/CC and $SnS_{2-x}O_x$/CC. Based on cyclic voltammogram measurements at different scan rates, the double-layer capacitance (C_{dl}) value increased from 3.27 mF cm^{-2} of the pristine SnS_2/CC to 3.75 mF cm^{-2} of the $SnS_{2-x}O_x$/CC, indicating that surface oxygen injection effectively increases the electrochemical active surface area (ECSA) of the electrocatalysts (Figs. S16 and S17). Given that the ECSA of the electrocatalysts is positively correlated with the active sites, we have reason to believe that the surface oxygen modification effectively exposes the active site of Sn. The Tafel plots were further employed to verify the rate-limiting step of the Sn-based catalysts in the CO_2RR process. The Tafel slopes of the Sn-based catalysts were all close to 118 mV dec^{-1},

demonstrating that the activation of CO_2 served as the rate-limiting step (Fig. S18) [34,35]. In addition, the Nyquist plots were used to confirm the facilitated electron transfer process [36]. The $SnS_{2-x}O_x$/CC displayed the charge transfer resistance (R_{CT}) of 12.1 Ω, which was smaller than that (15.8 Ω) of SnS_2/CC (Fig. S19). Therefore, surface oxygen injection effectively accelerates the charge transfer process of SnS_2/CC during the CO_2RR (Fig. 3).

3.3 *Operando* X-ray Absorption Spectroscopy Study

Given that the bulk phase stability of transition metal chalcogenides with heat treatment is destroyed, the bulk phase is in a relatively unstable state [37]. Based on the equilibrium theory of crystalline chemistry, the catalyst in the electrolyte driven by both energetical and kinetical force will tend to freely optimize the structure of the entire bulk, so that the bulk tends to a relatively stable state [38–41]. Therefore, we employed *operando* XAFS measurements to monitor the structural evolutions of the $SnS_{2-x}O_x$/CC under realistic working conditions. Figure 4a shows the *operando* Sn K-edge XANES spectra at different applied potentials, along with the data for Sn foil, SnS_2, and SnO_2 as references. When cathodic potentials were applied, the absorption edge of Sn K-edge XANES spectra shifted toward low-E side compared to the case of the open-circuit condition, indicating the decrease in the Sn valence state during CO_2RR process. Furthermore, when a cathodic potential of -0.9 V versus RHE was applied, the white line peak intensity was significantly increased in relation to the case (-0.4 V versus RHE), indicating more 5p electrons participate in the reaction. After the reaction, the white line peak approximately returned to the state (-0.4 V versus RHE), further confirming that the $SnS_{2-x}O_x$/CC catalyst undergone in situ reconstruction during the reaction and tended to form a relatively stable state.

Furthermore, the EXAFS was further employed to reveal the atomic reconstruction of the $SnS_{2-x}O_x$/CC catalyst under working conditions (Figs. 4b and S20). At first sight, the Fourier transform curves of $SnS_{2-x}O_x$/CC displayed a significantly dampening in the Sn-S coordination peak and a heightening in the Sn-nonmetallic coordination peak under working condition. Specifically, at the applied potential of -0.4 V versus RHE before the occurrence of CO_2RR, the
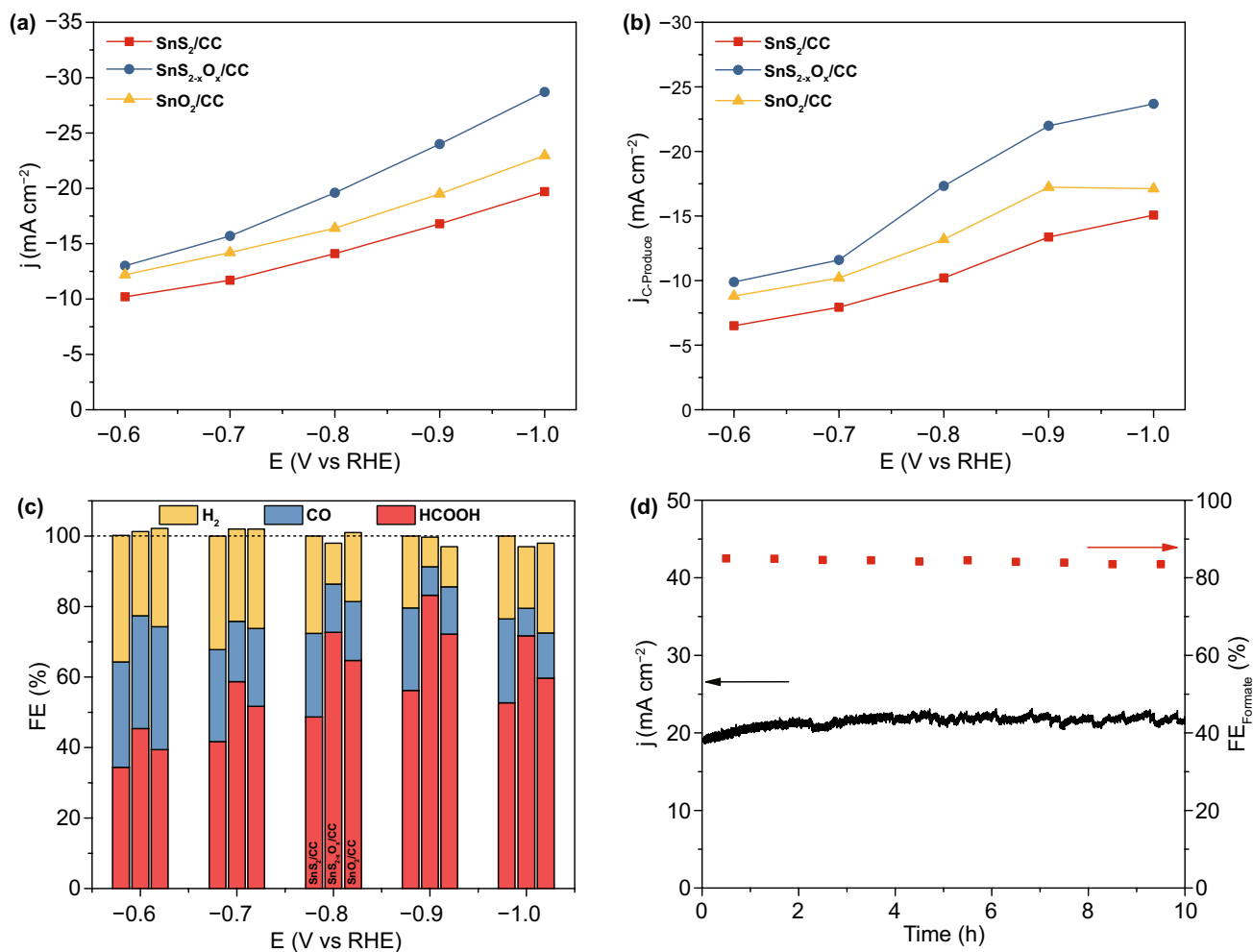
Fig. 3 **a** Geometrical current densities over SnS_2/CC, $SnS_{2-x}O_x$/CC, and SnO_2/CC. **b** Current densities for carbonaceous product (C-product) over SnS_2/CC, $SnS_{2-x}O_x$/CC, and SnO_2/CC. **c** Faradaic efficiencies for formate, H_2, and CO production over SnS_2/CC, $SnS_{2-x}O_x$/CC, and SnO_2/CC. **d** Plot of geometrical current density (j) and Faradaic efficiencies for C-product versus time over the $SnS_{2-x}O_x$/CC at a constant potential of −0.9 V vs RHE

EXAFS fitting results showed that the Sn–O coordination number increased from 2.5 to 3.6, which may be ascribed to the further doping of surface oxygen into the SnS_2 lattice during the reaction. To further verify the above conjecture, we performed XRD on the $SnS_{2-x}O_x$/CC after reaction. As expected, the intensity of the diffraction peaks of SnS_2 was significantly reduced after the reaction, and the characteristic peak of SnO_2 appeared in the $SnS_{2-x}O_x$/CC after reaction (Fig. S21). Moreover, at the potential of -0.9 V versus RHE during CO_2RR, Sn–O coordination number arose from 3.6 to 4.2 and the Sn-S coordination number remained unchanged, which may be attributed to the adsorption of the reaction intermediate species. When the cathode potential was removed, the Sn–O coordination number recovered to the state at −0.4 V, while the coordination number of Sn–S remained unchanged (Table S2). The above results indicated that the $SnS_{2-x}O_x$/CC had undergone dynamic surface reconstruction and surface oxygen doping plays a critical role under reaction conditions.
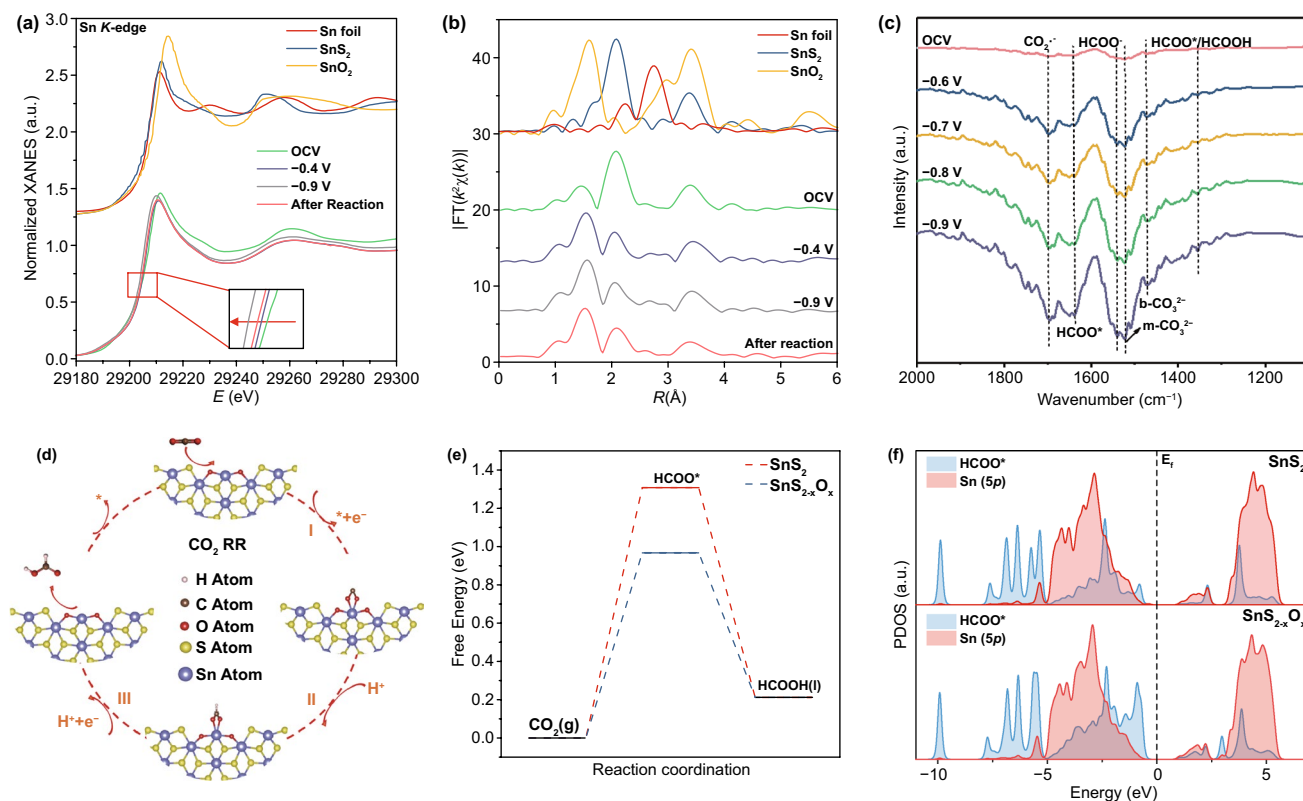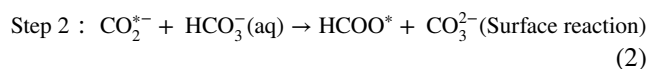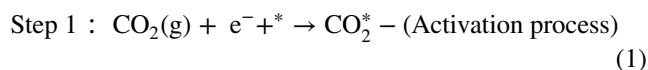
Fig. 4 **a** *Operando* XANES spectra at the Sn K-edge. **b** *Operando* k^2-weighted FT spectra at the Sn K-edge. **c** *Operando* SR-FTIR spectra of the SnS$_{2-x}$O$_x$/CC under the working condition. **d** Schematic of the whole CO$_2$RR mechanism on SnS$_{2-x}$O$_x$ nanosheets. **e** Gibbs free energy diagrams for CO$_2$ reduction to HCOOH on SnS$_2$ and SnS$_{2-x}$O$_x$ slabs. **f** Projected density of states (PDOS) of HCOO* adsorbed on the SnS$_2$ and SnS$_{2-x}$O$_x$ slabs. The * represents an adsorption site
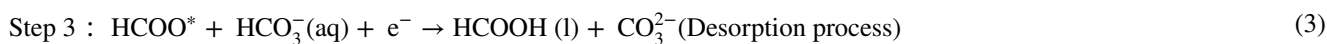
3.4 *Operando* Synchrotron Radiation Fourier Transform Infrared Spectroscopy Study

Operando synchrotron radiation Fourier transform infrared spectroscopy (SR-FT-IR) was further employed to investigate the catalytic mechanism for the well-designed SnS$_{2-x}$O$_x$/CC during the CO$_2$RR. All SR-FTIR spectra were recorded with the electrocatalysts at CO$_2$RR catalytic process (open circuit, -0.6, -0.7, -0.8, and -0.9 V) to reveal the production and transformation of key intermediates. As displayed in Fig. 4c, the monodentate carbonate groups (m-CO$_3^{2-}$) appeared at the peaks of ~ 1520 cm^{-1}, demonstrating that more CO$_2$ was adsorbed on the surface of electrocatalyst with the decrease in applied voltage. Meanwhile, a new characteristic peak appeared in the SR-FTIR spectra of ~ 1694 cm^{-1} (CO$_2 \cdot^-$ radicals) and the intensity of peak continually increased as the applied potentials decreased,

indicating that the CO$_2$ molecules adsorbed on the catalyst surface were activated to CO$_2 \cdot^-$ radicals during the reaction [42]. Meanwhile, as the cathode potential decreases, the peak intensity at ~ 1541 cm^{-1} (HCOO$^-$) increased further confirming the excellent proton trapping ability of CO$_2 \cdot^-$ radicals [33]. The peaks at ~ 1354 cm^{-1} and ~ 1660 cm^{-1} is ascribed to the symmetry vibration of the HCOO* intermediates, which corresponds to the key intermediates or the products for CO$_2$ electroreduction [43]. Based on the above-mentioned operando SR-FTIR analysis, the pathway of electroreduction from CO$_2$-to-HCOOH conversion by the SnS$_{2-x}$O$_x$/CC could be proposed as the following reactions (Fig. 4d):

Step 1 : $\text{CO}_2(g) + e^- +^* \rightarrow \text{CO}_2^* - $ (Activation process)

(1)

Step 2 : $\text{CO}_2^{*-} + \text{HCO}_3^-(aq) \rightarrow \text{HCOO}^* + \text{CO}_3^{2-}$ (Surface reaction)

(2)

Step 3 ：$HCOO^* + HCO_3^-(aq) + e^- \rightarrow HCOOH(l) + CO_3^{2-}$ (Desorption process) $\qquad$ (3)

3.5 Density Functional Theory (DFT) Calculations

DFT calculations were employed to elucidate the catalytic contribution from partial oxidation at $SnS_{2-x}O_x$ for CO_2RR. The models for pristine SnS_2 and $SnS_{2-x}O_x$ were chosen for the simulation. Figure S22 shows optimized adsorption configurations of HCOO* intermediates on the armchair edges of the pristine SnS_2 slab and SnS_2O_x slab with distinguishable Sn-O distances. from the material [44]. Specifically, the Sn–O bond length (d_{Sn-O}) is 2.28 Å for SnS_2, while the bond length d_{Sn-O} for $SnS_{2-x}O_x$ is reduced to 2.24 Å, implying that the surface oxygen injection effectively enhances the binding to the HCOO* intermediate. Besides, DFT calculations were further conducted on the Gibbs free energy (ΔG) with multiple elementary reaction steps over SnS_2 with/without oxygen injection. As exhibited in Fig. 4e, for both SnS_2 and $SnS_{2-x}O_x$, the formation of HCOO* is further confirmed to be the rate-limiting step for formate, which is consistent with the results of Tafel slopes. For the $SnS_{2-x}O_x$ slab, the ΔG for HCOO* formation (ΔG_{HCOO^*}) was calculated to be 0.97 eV, which is much lower than that for pristine SnS_2 slab (1.31 eV), indicating surface oxygen injection enhanced the activation of CO_2 and correspondingly facilitated the formation of HCOO*. To gain an in-depth insight into the nature of surface oxygen doping enhancing the intrinsic activity of SnS_2, we calculated the projected density of state of HCOO* absorbed SnS_2 and $SnS_{2-x}O_x$ (Fig. 4f). In the HCOO* PDOS, the dominant features are that HCOO* exhibits strong interaction with the valence band region of SnS_2 and $SnS_{2-x}O_x$, which leads to strong chemical adsorption. Notably, the state density of HCOO* overlaps more with the orbital of Sn (5p) in $SnS_{2-x}O_x$ with regard to that in SnS_2, and the higher occupied state of HCOO* is near the Fermi level, indicating that HCOO* has a stronger interaction with $SnS_{2-x}O_x$, which is consistent with the calculation result of ΔG_{HCOO^*}. Furthermore, the charge density differences calculations also show that more electrons gather around the adsorption site in $SnS_{2-x}O_x$, indicating that the surface oxygen injection makes the SnS_2 edges exhibit a stronger affinity for HCOO* species (Fig. S23). The above results confirm that surface oxygen injection alters the local electronic structure of Sn atom with optimal ΔG_{HCOO^*} to effectively facilitate the production of formate over CO_2RR.

Particularly, the above theoretical calculation results are consistent with the previous experimental results.

4 Conclusions

In conclusion, we developed SnS_2 nanosheets with surface oxygen modification for CO_2 electroreduction to formate and syngas (CO and H_2). The surface oxygen-injection engineering achieved exposure of Sn active site and optimal Sn electronic states, thereby enhancing the adsorption and activation of CO_2. Surface oxygen injection on SnS_2 nanosheets significantly improved electrocatalytic activity and selectivity of CO_2 reduction to formate and syngas (CO and H_2). Specifically, at −0.9 V vs RHE, the $SnS_{2-x}O_x$/CC exhibits the highest FE of 91.6% for carbonaceous products, including the FE of 83.2% for formate production and the FE of 16.5% for syngas with the H_2/CO ratio of 1:1. Moreover, the as-prepared $SnS_{2-x}O_x$/CC displays an excellent durability for 10-h potentiostatic test with less than 4% decay in current density. *Operando* XAS unravels that the in situ surface oxygen doping into the matrix under working conditions effectively modulates the Sn local electronic state. *Operando* SR-FTIR and DFT calculations reveal that the surface oxygen doping enhanced the affinity for HCOO* species by manipulating the Sn electronic states and accelerated the CO_2 activation. This work opens a span-new door for the design of advanced catalysts for CO_2 electroreduction.

Author Contributions TC, TY, and WZ developed the idea and designed experiments. TC, XS, WZ, LW, and TD performed the catalyst synthesis and characterizations and FTIR measurements and electrochemical experiments. LC and TD performed the TEM characterization. WZ and XL made the XAFS calculation and analysis on Sn *K*-edge. TC and TY co-wrote the paper. TL and QL performed the DFT calculations. All authors discussed the results and commented on the manuscript.

References

1. H. Li, C. Qiu, S. Ren, Q. Dong, S. Zhang et al., Na$^+$-gated water-conducting nanochannels for boosting CO_2 conversion to liquid fuels. Science **367**(6478), 667–671 (2020). https://doi.org/10.1126/science.aaz6053

2. J. Gu, C-S. Hsu, L. Bai, H.M. Chen, X. Hu, Atomically dispersed f Fe^{3+} sites catalyze efficient CO_2 electroreduction to CO. Science **364**(6445), 1091–1094 (2019). https://doi.org/10.1126/science.aaw7515

3. T. Möller, F. Scholten, T.N. Thanh, I. Sinev, J. Timoshenko et al., Electrocatalytic CO_2 reduction on cuox nanocubes: tracking the evolution of chemical state, geometric structure, and catalytic selectivity using operando spectroscopy. Angew. Chem. Int. Ed. **132**(41), 18130–18139 (2020). https://doi.org/10.1002/anie.202007136

4. K. Jiang, Y. Huang, G. Zeng, F.M. Toma, W.A. Goddard et al., Effects of surface roughness on the electrochemical reduction of CO_2 over Cu. ACS Energy Lett. **5**(4), 1206–1214 (2020). https://doi.org/10.1021/acsenergylett.0c00482

5. W. Ma, S. Xie, T. Liu, Q. Fan, J. Ye et al., Electrocatalytic reduction of CO_2 to ethylene and ethanol through hydrogen-assisted C-C coupling over fluorine-modified copper. Nat. Catal. **3**(6), 478–487 (2020). https://doi.org/10.1038/s41929-020-0450-0

6. Q. Gong, P. Ding, M. Xu, X. Zhu, M. Wang et al., Structural defects on converted bismuth oxide nanotubes enable highly active electrocatalysis of carbon dioxide reduction. Nat. Commun. **10**(1), 2807 (2019). https://doi.org/10.1038/s41467-019-10819-4

7. G. Wen, D.U. Lee, B. Ren, F.M. Hassan, G. Jiang et al., Orbital interactions in Bi-Sn bimetallic electrocatalysts for highly selective electrochemical CO_2 reduction toward formate production. Adv. Energy Mater. **8**(31), 1802427 (2018). https://doi.org/10.1002/aenm.201802427

8. X. Wei, Y. Li, L. Chen, J. Shi, Formic acid electro-synthesis by concurrent cathodic CO_2 reduction and anodic CH_3OH oxidation. Angew. Chem. Int. Ed. **60**(6), 3148–3155 (2021). https://doi.org/10.1002/anie.202012066.

9. Y. Xing, X. Kong, X. Guo, Y. Liu, Q. Li et al., Bi@Sn core–shell structure with compressive strain boosts the electroreduction of CO_2 into formic acid. Adv. Sci. **7**(22), 1902989 (2020). https://doi.org/10.1002/advs.201902989

10. F. Li, L. Chen, M. Xue, T. Williams, Y. Zhang et al., Towards a better Sn: Efficient electrocatalytic reduction of CO_2 to formate by Sn/SnS_2 derived from SnS_2 nanosheets. Nano Energy **31**, 270–277 (2017). https://doi.org/10.1016/j.nanoen.2016.11.004

11. J. Xu, S. Lai, M. Hu, S. Ge, R. Xie et al., Semimetal $1H-SnS_2$ enables high-efficiency electroreduction of CO_2 to CO. Small Methods **4**(10), 2000567 (2020). https://doi.org/10.1002/smtd.202000567

12. X. Li. S. Dou, J. Wang, X., Investigation of structural evolution of SnO_2 nanosheets towards electrocatalytic CO_2 reduction. Chem. Asian J. **15**, 1558–1561 (2020). https://doi.org/10.1002/asia.202000252

13. X. Zheng, P. De Luna, F.P. García de Arquer, B. Zhang, N. Becknell et al., Sulfur-modulated tin sites enable highly selective electrochemical reduction of CO_2 to formate. Joule **1**(4), 794–805 (2017). https://doi.org/10.1016/j.joule.2017.09.014

14. Z. Li, A. Cao, Q. Zheng, Y. Fu, T. Wang et al., Elucidation of the synergistic effect of dopants and vacancies on promoted selectivity for CO_2 electroreduction to formate. Adv. Mater. **33**(2), 2005113 (2021). https://doi.org/10.1002/adma.202005113

15. J. Wang, S. Ning, M. Luo, D. Xiang, W. Chen et al., In-Sn alloy core-shell nanoparticles: In-doped snox shell enables high stability and activity towards selective formate production from electrochemical reduction of CO_2. Appl. Catal. B: Environ. **288**, 119979 (2021). https://doi.org/10.1016/j.apcatb.2021.119979

16. J. Wu, Y. Xie, S. Du, Z. Ren, P. Yu et al., Heterophase engineering of SnO_2/Sn_3O_4 drives enhanced carbon dioxide electrocatalytic reduction to formic acid. Sci. China Mater. **63**(11), 2314–2324 (2020). https://doi.org/10.1007/s40843-020-1361-3

17. C. Hu, L. Zhang, L. Li, W. Zhu, W. Deng et al., Theory assisted design of n-doped tin oxides for enhanced electrochemical CO_2 activation and reduction. Sci. China Mater. **62**(8), 1030–1036 (2019). https://doi.org/10.1007/s11426-019-9474-0

18. W. Zhang, P. He, C. Wang, T. Ding, T. Chen et al., Operando evidence of Cu^+ stabilization via a single-atom modifier for CO_2 electroreduction. J. Mater. Chem. A **8**(48), 25970–25977 (2020). https://doi.org/10.1039/D0TA08369K

19. W. Guo, X. Tan, J. Bi, L. Xu, D. Yang et al., Atomic indium catalysts for switching CO_2 electroreduction products from formate to CO. J. Am. Chem. Soc. **143**(18), 6877–6885 (2021). https://doi.org/10.1021/jacs.1c00151

20. I. Grigioni, L.K. Sagar, Y.C. Li, G. Lee, Y. Yan et al., CO_2 electroreduction to formate at a partial current density of 930 mA cm^{-2} with inp colloidal quantum dot derived catalysts.

ACS Energy Lett. **6**(1), 79–84 (2021). (https://doi.org/10.1021/acsenergylett.0c02165

21. R. Pang, P. Tian, H. Jiang, M. Zhu, X. Su et al., Tracking structural evolution: Operando regenerative CeO_x/Bi interface structure for high-performance CO_2 electroreduction. Nat. Sci. Rev. nwaa187 (2020). https://doi.org/10.1093/nsr/nwaa187

22. F. Yang, X. Ma, W.-B. Cai, P. Song, W. Xu, Nature of oxygen-containing groups on carbon for high-efficiency electrocatalytic CO_2 reduction reaction. J. Am. Chem. Soc. **141**(51), 20451–20459 (2019). https://doi.org/10.1021/jacs.9b11123

23. H. Li, N. Xiao, Y. Wang, C. Li, X. Ye et al., Nitrogen-doped tubular carbon foam electrodes for efficient electroreduction of CO_2 to syngas with potential-independent CO/H_2 ratios. J. Mater. Chem. A **7**(32), 18852–18860 (2019). https://doi.org/10.1039/C9TA05904K

24. R. Daiyan, E.C. Lovell, B. Huang, M. Zubair, J. Leverett et al., Uncovering atomic-scale stability and reactivity in engineered zinc oxide electrocatalysts for controllable syngas production. Adv. Energy Mater. **10**(28), 2001381 (2020). https://doi.org/10.1002/aenm.202001381

25. X. Wang, Z. Wang, F.P. Garcia de Arquer, C.-T. Dinh, A. Ozden et al., Efficient electrically powered CO_2-to-ethanol via suppression of deoxygenation Nat. Energy **5**(6), 478–486 (2020). https://doi.org/10.1038/s41560-020-0607-8

26. M.S. Xie, B.Y. Xia, Y. Li, Y. Yan, Y. Yang et al., Amino acid modified copper electrodes for the enhanced selective electroreduction of carbon dioxide towards hydrocarbons. Energy Environ. Sci. **9**(5), 1687–1695 (2016). https://doi.org/10.1039/C5EE03694A

27. J. Jeong, J.S. Kang, H. Shin, S.H. Lee, J. Jang et al., Self-supported mesoscopic tin oxide nanofilms for electrocatalytic reduction of carbon dioxide to formate. Chem. Commun. **57**(28), 3445–3448 (2021). https://doi.org/10.1039/D1CC00927C

28. S. Gao, Y. Lin, X. Jiao, Y. Sun, Q. Luo et al., Partially oxidized atomic cobalt layers for carbon dioxide electroreduction to liquid fuel. Nature **529**(7584), 68–71 (2016). https://doi.org/10.1038/nature16455

29. D.H. Won, C.H. Choi, J. Chung, M.W. Chung, E.-H. Kim et al., Rational design of a hierarchical tin dendrite electrode for efficient electrochemical reduction of CO_2. CheSusChem **8**(18), 3092–3098 (2015). https://doi.org/10.1002/cssc.201500694

30. Y. Wang, Y. W.u, X. Liu, H. Zhang, M. Zhou et al., Atomic sandwiched p-n homojunctions. Angew. Chem. Int. Ed. **60**, 3487 (2020). https://doi.org/10.1002/anie.202012734

31. A. Zhang, R. He, H. Li, Y. Chen, T. Kong et al., Nickel doping in atomically thin tin disulfide nanosheets enables highly efficient CO_2 reduction. Angew. Chem. Int. Ed. **130**(34), 11120–11124 (2018). https://doi.org/10.1002/ange.201806043

32. M.F. Baruch, J.E. Pander III, J.L. White, A.B. Bocarsly, Mechanistic insights into the reduction of CO_2 on tin electrodes using in situ ATR-IR spectroscopy. ACS Catal. **5**(5), 3148–3156 (2015). https://doi.org/10.1021/acscatal.5b00402

33. H. Cheng, S. Liu, J. Zhang, T. Zhou, N. Zhang et al., Surface nitrogen-injection engineering for high formation rate of CO_2 reduction to formate. Nano Lett. **20**(8), 6097–6103 (2020). https://doi.org/10.1021/acs.nanolett.0c02144

34. Z. Zhang, F. Ahmad, W. Zhao, W. Yan, W. Zhang et al., Enhanced electrocatalytic reduction of CO_2 via chemical coupling between indium oxide and reduced graphene oxide. Nano Lett. **19**(6), 4029–4034 (2019). https://doi.org/10.1021/acs.nanolett.9b01393

35. A. Zhang, Y. Liang, H. Li, X. Zhao, Y. Chen et al., Harmonizing the electronic structures of the adsorbate and catalysts for efficient CO_2 reduction. Nano Lett. **19**(9), 6547–6553 (2019). https://doi.org/10.1021/acs.nanolett.9b02782

36. Z. Chen, M.-R. Gao, N. Duan, J. Zhang, Y.-Q. Zhang et al., Tuning adsorption strength of CO_2 and its intermediates on tin oxide-based electrocatalyst for efficient CO_2 reduction towards carbonaceous products. Appl. Catal. B: Environ. **277**, 119252 (2020). https://doi.org/10.1016/j.apcatb.2020.119252

37. K. Fan, H. Zou, Y. Lu, H. Chen, F. Li et al., Direct observation of structural evolution of metal chalcogenide in electrocatalytic water oxidation. ACS Nano **12**(12), 12369–12379 (2018). https://doi.org/10.1021/acsnano.8b06312

38. S. Jin, Are metal chalcogenides, nitrides, and phosphides oxygen evolution catalysts or bifunctional catalysts? ACS Energy Lett. **2**(8), 1937–1938 (2017). https://doi.org/10.1021/acsenergylett.7b00679

39. A. Dutta, A.K. Samantara, S.K. Dutta, B.K. Jena, N. Pradhan, Surface-oxidized dicobalt phosphide nanoneedles as a nonprecious, durable, and efficient oer catalyst. ACS Energy Lett. **1**(1), 169–174 (2016). https://doi.org/10.1021/acsenergylett.6b00144

40. A. Sivanantham, P. Ganesan, A. Vinu, S. Shanmugam, Surface activation and reconstruction of non-oxide-based catalysts through in situ electrochemical tuning for oxygen evolution reactions in alkaline media. ACS Catal. **10**(1), 463–493 (2020). https://doi.org/10.1021/acscatal.9b04216

41. O. Mabayoje, A. Shoola, B.R. Wygant, C.B. Mullins, The role of anions in metal chalcogenide oxygen evolution catalysis: electrodeposited thin films of nickel sulfide as "pre-catalysts". ACS Energy Lett. **1**(1), 195–201 (2016). https://doi.org/10.1021/acsenergylett.6b00084

42. L. Liu, Y. Jiang, H. Zhao, J. Chen, J. Cheng et al., Engineering coexposed {001} and {101} facets in oxygen-deficient TiO2 nanocrystals for enhanced CO2 photoreduction under visible light. ACS Catal. **6**(2), 1097–1108 (2016). https://doi.org/10.1021/acscatal.5b02098

43. W. Zhang, Y. Hu, L. Ma, G. Zhu, Y. Wang et al., Progress and perspective of electrocatalytic CO_2 reduction for renewable carbonaceous fuels and chemicals. Adv. Sci. **5**(1), 1700275 (2018). https://doi.org/10.1002/advs.201700275

44. H. Yang, Y. Hu, J. Chen, M.S. Balogun, P. Fang et al., Intermediates adsorption engineering of CO2 electroreduction reaction in highly selective heterostructure Cu-based electrocatalysts for CO production. Adv. Energy Mater. **9**(27), 1901396 (2019). https://doi.org/10.1002/aenm.201901396